Downloaded from ascelibrary.org by Ecole Polytechnique Federale de Lausanne on 01/20/22. Copyright ASCE. For personal use only; all rights reserved.

# Inverse Analysis of R-UHPFRC Beams to Determine the Flexural Response under Service Loading and at Ultimate Resistance

Bartłomiej Sawicki, D.Sc.[1]; Eugen Brühwiler, D.Sc.[2]; and Emmanuel Denarié, D.Sc.[3]

**Abstract:** Ultra high performance fiber reinforced cementitious composites (UHPFRCs) have demonstrated their outstanding efficiency as structural materials. Determination of the bending resistance of members combining UHPFRC with steel reinforcement bars (R-UHPFRC) using material properties obtained by material testing gives satisfactory results. However, the synergetic interaction between rebar and UHPFRC in the tensile action due to bending, especially under loading–unloading of the structure is not yet well understood. This paper compared methods of analytical inverse analyses, as well as finite-element modeling and nondestructive testing (NDT), for determining UHPFRC material properties based on plates and R-UHPFRC members' test results. It was demonstrated that UHPFRC in the tensile zone of R-UHPFRC members can enter into compression during unloading, influencing the structural response under service loading. **DOI: 10.1061/(ASCE)ST.1943-541X.0003239.** *This work is made available under the terms of the Creative Commons Attribution 4.0 International license, https://creativecommons.org/licenses/by/4.0/.*

**Author keywords:** Ultra high performance fiber reinforced cementitious composites (UHPFRC); Inverse analysis; Nondestructive testing (NDT); Serviceability; Resistance; Scatter.

## Introduction

Ultra high performance fiber reinforced cementitious composites (UHPFRCs) are a relatively new class of building materials (Naaman 2018). They are composed of a cementitious matrix with fine grains (<1 mm) and a high dosage of discontinuous short fibers, usually made of steel (>3% by volume) (Brühwiler 2016). This material often is combined with steel reinforcement bars to form reinforced UHPFRC (R-UHPFRC). The number of implementations in structural engineering to rehabilitate and strengthen existing structures and to design and build new structures is increasing rapidly in Switzerland (MCS EPFL 2020) and around the world (Azmee and Shafiq 2018; Graybeal et al. 2020; Yoo and Yoon 2016).

Most of the research on stress distribution in R-UHPFRC members has focused on the ultimate resistance (Adel et al. 2019; Farhat et al. 2007; Habel et al. 2007; Qiu et al. 2020) or monotonic loading (Huang et al. 2019; Yang et al. 2019), without taking into account unloading of the member. The structural response under service loading with an analytical method of taking into account change of stiffness due to loading–unloading was discussed by Gao et al. (2020), but without detailed analysis of stress distribution in the cross section or composite behavior between steel reinforcement bars and UHPFRC (Wang et al. 2020).

As far as the ultimate resistance of members determines structural safety, the serviceability state prevails during service duration of a structure. Understanding the behavior of a structure under loading–unloading conditions, for example, due to live loads, and taking into account intrinsic scatter of material properties in a structural member (Oesterlee et al. 2009) is necessary to eliminate discrepancies between modeled and measured responses (Brühwiler et al. 2019).

The principle of inverse analysis is based on modeling of an experiment, from which the material properties are indirectly retrieved. Using this method, the direct tensile test, which unequivocally is difficult to conduct, can be replaced by relatively simple bending tests. In this way, the inherent variation of UHPFRC properties in different elements (Oesterlee et al. 2009) can be quantified. Several inverse analysis methods are available, using simplified closed-form solutions (AFGC 2013; López et al. 2015, 2016; Qian and Li 2008) as well as numerical (Baby et al. 2013; de Oliveira e Sousa and Gettu 2006; Denarié et al. 2017), analytical (Baril et al. 2016), and finite-element methods (Mezquida-Alcaraz et al. 2019; Tailhan et al. 2004), taking into account scatter of material properties in members (Rossi et al. 2015). Inverse analysis also can be done for larger members (Pan et al. 2016; Shen et al. 2020). The present work used analytical and numerical finite-element modeling (FEM) methods.

The tensile strength of UHPFRC depends on fiber geometry, content, orientation, and the pull-out shear stress of fibers from the cementitious matrix (Naaman 2018; Oesterlee et al. 2009). Fiber content and orientation in a structural element can be determined using tomography or X-ray scanning (Barnett et al. 2010); however, these methods are impractical on-site. In the case of UHPFRC with steel fibers, their magnetic conductivity can be used to determine content and orientation in non-destructive way, and further link it

[1]Ex Ph.D. Student, Scientific Collabolator, Laboratory of Maintenance and Safety of Structures, Structural Engineering Institute, École Polytechnique Fédérale de Lausanne, CH-1015 Lausanne, Switzerland (corresponding author). ORCID: https://orcid.org/0000-0002-5632-3461. Email: bartek.sawicki@epfl.ch

[2]Professor, Head of Laboratory, Laboratory of Maintenance and Safety of Structures, Structural Engineering Institute, École Polytechnique Fédérale de Lausanne, CH-1015 Lausanne, Switzerland. Email: eugen.bruehwiler@epfl.ch

[3]Senior Scientist, Laboratory of Maintenance and Safety of Structures, Structural Engineering Institute, École Polytechnique Fédérale de Lausanne, CH-1015 Lausanne, Switzerland. Email: emmanuel.denarie@epfl.ch

Note. This manuscript was submitted on November 24, 2020; approved on September 15, 2021; published online on November 19, 2021. Discussion period open until April 19, 2022; separate discussions must be submitted for individual papers. This paper is part of the ***Journal of Structural Engineering***, © ASCE, ISSN 0733-9445.

with tensile strength (Nunes et al. 2016) resulting in magnetic nondestructive testing (NDT).

This study had two objectives: (1) to deduce the stress distribution in R-UHPFRC bent members under loading–unloading action, and (2) to observe the scatter of material performance in small and large UHPFRC elements. The following experiments were conducted: (1) magnetic NDT and four-point bending tests on full-scale R-UHPFRC beams; (2) standardized four-point bending tests on companion plates; and (3) magnetic NDT and four-point bending tests on thicker plates for calibration of the NDT method. Analytical and FEM inverse analysis methods were applied to determine material properties from bending tests of full-scale members and companion plate specimens. Obtained results were compared against results of magnetic NDT. The stress distribution in cross sections of R-UHPFRC beams under loading–unloading can be modeled precisely using the identified material properties. Finally, the results of modeling were validated with strain values of reinforcement bars measured during experiments.

This paper is structured as follows. Section "Methods" presents all the methods: (1) setups for testing of UHPFRC plates and R-UHPFRC beams, (2) analytical and numerical methods of inverse analysis, (3) constitutive model of UHPFRC under loading–unloading in tension, (4) numerical model for calculation of stress profiles, and (5) principles and calibration of magnetic NDT. In the section "UHPFRC Properties," properties of UHPFRC obtained using different methods are compared and discussed. In the section "Ultimate Resistance of Members," the importance of the variation of obtained material properties is quantified and compared with experiments using the bending resistance of R-UHPFRC beams. In the section "Stress Distribution in Members under Service Conditions," previously obtained material properties are used to calculate stress profiles in R-UHPFRC under loading–unloading; the results are validated with experiments.

## Methods

### *Testing of Flexural Members*

#### UHPFRC Plates

The Swiss guidelines for UHPFRC, SIA 2052 (Swiss Society of Engineers and Architects 2017), specify four-point bending tests of rectangular plates to obtain the tensile properties of UHPFRC by inverse analysis of experimental results. Plates of width $b_m$ and thickness $h_m$ are tested under four-point bending over a span $l_m$ with force application points spaced at $l_m/3$ (Fig. 1). Force and midspan deflection are recorded during testing. The material properties are obtained by inverse analysis methods.

#### R-UHPFRC Flexural Beams

In this paper, 10 beams of 3 different types (Fig. 2) are discussed; each member was cast separately. Three beams of Type 1, three beams of Type 2, and two beams of Type 3 were tested under quasi-static loading until failure. Additionally, one beam of Type 2 and one beam of Type 3 were tested under loading–unloading cycles to investigate the structural behavior under service conditions. The number of specimens of each type is presented in Table 1.

Beams of Type 1 contained one rebar of diameter Ø20 mm, and cover thickness $c_{\text{nom}} = 10$ mm, i.e., $\emptyset/2$. Beams of Type 2 were reinforced with one rebar with Ø34 mm and $c_{\text{nom}} = 17$ mm, i.e., $\emptyset/2$. Type 3 members contained one longitudinal rebar with Ø20 mm and $c_{\text{nom}} = 10$ mm, and Ω-shaped Ø6 mm stirrups (Fig. 2). Although Types 1 and 3 had the same longitudinal reinforcement (Ø20 mm), the rebars were fabricated and delivered separately, and thus they were treated separately.

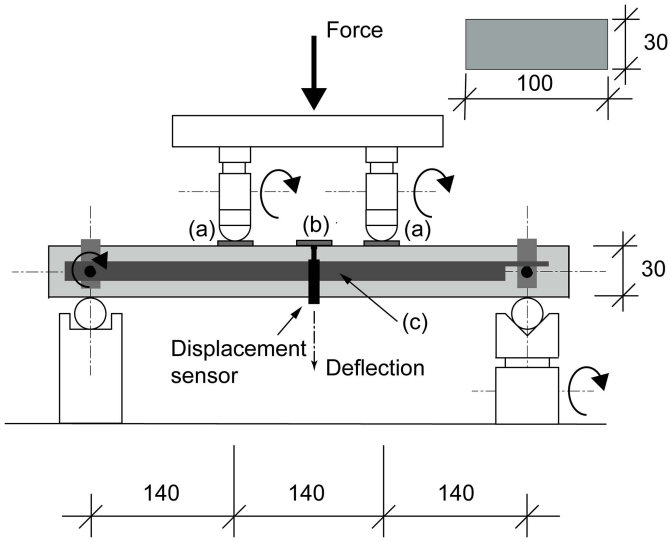


**Fig. 1.** Side view and cross-section of four-point bending test of plate specimens to determine the tensile properties of UHPFRC according to SIA 2052 (Swiss Society of Engineers and Architects 2017): (a) loading points; (b) deflection measurement point; and (c) deflection measurement reference frame. (Dimensions: mm.)

All the beams were cast in horizontal position (as tested), pouring fresh UHPFRC from the top at one end. Six external vibrators attached to walls of the formwork assured good flow of the mix. After casting, the formworks were covered with foil for 7 days. Then the beams were unmolded, wrapped in foil, and transported to storage area.

The beams were subjected to quasi-static displacement-controlled four-point bending tests. The constant bending moment zone varied between 0.2 and 0.7 m (Fig. 2), to ensure bending failure mode rather than shear failure. The displacement was applied using a servohydraulic actuator and transmitted using a hinge and a steel beam. The resultant force was measured using the load cell of the actuator. For Groups 2 and 3, foil strain gauges (SGs) were glued on rebars at midspan and ±200 mm from midspan before casting.

Commercially available UHPFRC mix Holcim710 (Holcim (Schweiz) AG (Zürich, Switzerland) was used, with 3.8% by volume 13-mm straight steel fibers with an aspect ratio of 65. The minimum age at the moment of testing was 3 months. The cement hydration in UHPFRC is in an advanced stage after 28 days and stops almost completely after 90 days (Habel et al. 2006), and thus it was assumed that the age had no influence on the material properties. To verify this, the companion plates were tested under four-point bending at 28 and 90 days after casting, which is discussed subsequently.

The mean compressive strength obtained by testing of 70 × 140-mm cylinders in direct compression at 28 days according to the Swiss standard was $f_{Uc} = 140.7$ MPa.

Both longitudinal reinforcement and stirrups were of type B500B according to the Swiss standard SIA 262 (SIA 2014) and Eurocode EC2 (BSI 2005), with theoretical characteristic yielding strength $f_{sk} = 500$ MPa. The properties of longitudinal reinforcement obtained using direct tension test according to Swiss standard are presented in Table 2. The rebars used in Type 1 beams had higher strength; however, they still met the requirements of B500B reinforcement class.





Downloaded from ascelibrary.org by Ecole Polytechnique Federale de Lausanne on 01/20/22. Copyright ASCE. For personal use only; all rights reserved.

Downloaded from ascelibrary.org by Ecole Polytechnique Federale de Lausanne on 01/20/22. Copyright ASCE. For personal use only; all rights reserved.

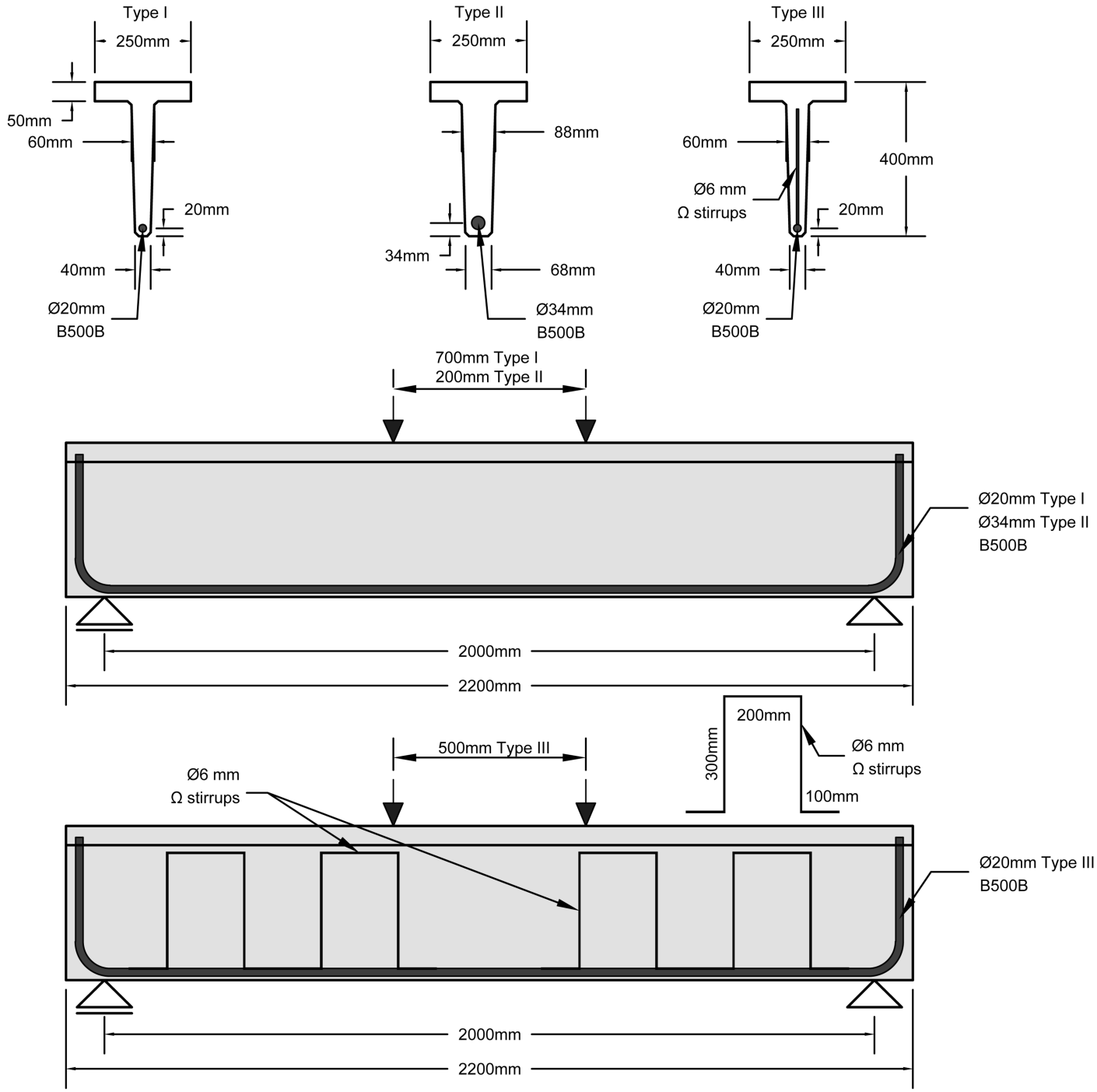


**Fig. 2.** Three types of beams tested under four-point bending.

**Table 1.** Number and types of R-UHPFRC beams and accompanying UHPFRC plates

| Beam type | Loading to failure | Loading–unloading | Plates, 28 days | Plates, 90 days |
|---|---|---|---|---|
| Type 1 (Ø20 mm) | 3 | 0 | 12 | 12 |
| Type 2 (Ø34 mm) | 3 | 1 | 6 | 6 |
| Type 3 (Ø20 mm) | 2 | 1 | 6 | 6 |

**Table 2.** Mean tensile material properties of reinforcement bars based on axial tensile tests

| Beam type | $f_s$ (MPa) | $f_t$ (MPa) | $\varepsilon_u$ (%) | $E_s$ (GPa) |
|---|---|---|---|---|
| Type 1 (Ø20 mm) | 600 | 687 | 9.2 | 224 |
| Type 2 (Ø34 mm) | 525 | 624 | 9.4 | 245 |
| Type 3 (Ø20 mm) | 512 | 617 | 9.2 | 234 |

Note: $f_s$ = yielding strength; $f_t$ = tensile strength; $\varepsilon_u$ = strain at rupture; and $E_s$ = modulus of elasticity.

Downloaded from ascelibrary.org by Ecole Polytechnique Federale de Lausanne on 01/20/22. Copyright ASCE. For personal use only; all rights reserved.

## *Inverse Analysis*

### Analytical Methods

Inverse analysis methods for an element under four-point bending are based on sectional stress distribution. Stress and strain values are sought for three points on the force–deflection curve [Fig. 3(a), A, B, and C].

Point A indicates the end of linearity of the force ($F$)–deflection ($\delta$) curve, implying loss of elasticity of the material. Sectional stress distribution and deflection at this point can be calculated using elasticity theory, obtaining Young's modulus $E_U$ and elastic limit stress $f_{Ute}$. Alternatively, $E_U$ can be calculated for each $F$-$\delta$ pair. Point A is the point at which an irreversible decrease of $E_U$ occurs.

The ultimate resistance of the element is reached at Point C. Using a stress block in tension and elastic response in compression for UHPFRC, knowing both the position of the neutral axis and the acting bending moment, and employing the sectional force equilibrium, the tensile strength of UHPFRC, $f_{Utu}$, is found [Fig. 3(c)]. In the case of R-UHPFRC members, the contribution of the reinforcement bar is taken into account as well.

Point B marks the moment at which softening behavior of UHPFRC comes into play. It is detected with iterative methods to identify the loss of agreement between the experimental deflection–force curve and that obtained analytically using a simplified material model with stress cut off at $f_{Utu}$. The lack of agreement indicates loss of validity of the model without postpeak resistance, and thus beginning of the softening behavior contribution of UHPFRC in bending resistance.

**Plates, Method 1**. The analytical inverse analysis method described in the Swiss UHPFRC recommendations, SIA 2052 (Swiss Society of Engineers and Architects 2017), was proposed by Denarié et al. (2017). This method is based on finding the three points A, B, and C separately.

To determine Point A, apparent secant moduli $E_i$ are found for each $\delta_i$-$F_i$ pair according to

$$E_i = 0.0177 \cdot \frac{F_i}{\delta_i} \cdot \frac{12 \cdot l_m^3}{b_m \cdot h_m^3} \tag{1}$$

The moving average $E_{mi}$ over 20 values of $E_i$ is computed, and the $\delta_i$-$E_{mi}$ curve is plotted. Point A corresponds to the deflection at Point A ($\delta_A$) for which an irreversible decrease of more than 1% of the value $E_{mi}$ occurs. The modulus of elasticity $E_U$ is equal to $E_{mi}$ at Point A, and the elastic limit stress $f_{Ute}$ is calculated by taking $F_A$ at this point and assuming linear elastic stress distribution over the section

$$f_{Ute} = \frac{F_A \cdot l_m}{b_m \cdot h_m^2} \tag{2}$$

A simplified formula to obtain $f_{Utu}$ is used at Point C. It is based on the following assumptions: sectional force equilibrium, linear elasticity of material in compression, and the neutral axis at $0.82h_m$ for this geometry of specimen. These assumptions were confirmed by direct tensile tests and numerical modeling (Denarié et al. 2017)

$$f_{Utu} = 0.383 \cdot \frac{F_C \cdot l_m}{b_m \cdot h_m^2} \tag{3}$$

To detect Point B, the curvature in the constant moment zone is assumed to remain proportional up to the peak force according to (AFGC 2013)

$$\chi_i = \frac{216}{23} \cdot \frac{\delta_i}{l_m^2} \tag{4}$$

For each pair $\delta_i$-$F_i$ the bending moment $M_i$ and further the tensile stress $\sigma_{Uti}$ and strain $\varepsilon_{Uti}$ on the bottom face of the specimen in the constant bending moment zone are computed according to

$$M_i = \frac{F_i \cdot l_m}{6} \tag{5}$$

$$\sigma_{Uti} = 0.5(1-\alpha_i)^2 h_m \chi_i E_U \tag{6}$$

$$\varepsilon_{Uti} = \frac{\sigma_{Uti}}{E_U} + \chi_i \alpha_i h_m \tag{7}$$

For simplification, the parameter $\lambda_i$ is defined by the following equation:

$$\lambda_i = \frac{12 M_i}{\chi_i E_U b_m h_m^3} \tag{8}$$

Equilibrium in the cross section yields

$$2\alpha_i^3 - 3\alpha_i^2 + 1 - \lambda_i = 0 \tag{9}$$

These values are computed for a series of points evenly distributed between Points A and C. At least 10 points are recommended, and the first point should be taken such that $\lambda_i = 0.5$ ($\alpha = 0.5$) to obtain a representative result for the whole cross section. The first point subscript $j$ for which the calculated $\sigma_{Utj} > f_{Utu}$ is taken as Point C, and thus the value of strain-hardening deformation of UHPFRC is $\varepsilon_{Utu} = \varepsilon_{Utj}$.

**Plates, Method 2**. The second method of inverse analysis for plates uses the same principles, but Points A and B are determined

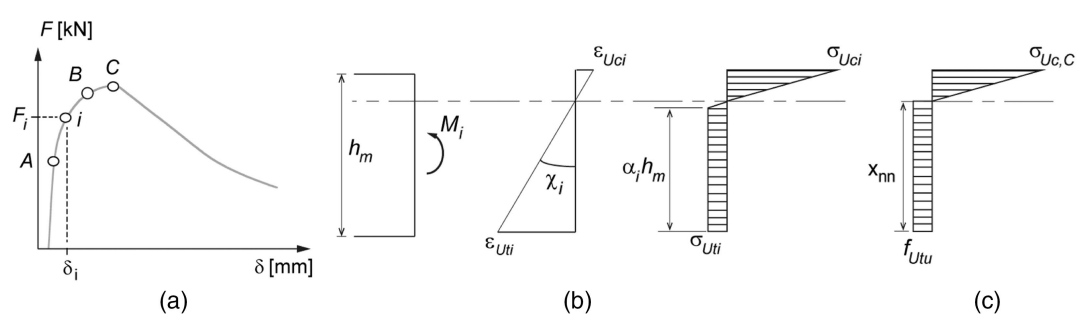


**Fig. 3.** Principle of inverse analysis of four-point bending test.

together, and the whole force–deflection curve is fitted between them (E. Denarié, personal communication, 2020).

First, the tensile strength $f_{Utu}$ is calculated using Eq. (3). Then the $F$-$\delta$ curve is computed on the basis of the assumed material properties. A set of $\alpha$ values (Fig. 3) is prepared. The minimum recommended number of points is 10. The points should range from $\alpha = 0$ (elastic state) to an $\alpha$-value such that the stress on the bottom face in the constant bending moment zone becomes $\sigma_{Uti} > f_{Utu}$.

For each point, the neutral axis position in relation to the specimen height is calculated based on force equilibrium, and

$$x_{n-n,i} = 0.5 + \frac{\lambda_i^2}{2}\left(1 - \frac{E_{Uh}}{E_U}\right) \tag{10}$$

where the hardening secant is computed as

$$E_{Uh} = \frac{f_{Utu} - f_{Ute}}{\varepsilon_{Utu} - \frac{f_{Utu}}{E_U}} \tag{11}$$

The curvature in the constant bending zone is

$$\chi_i = \frac{\frac{f_{Ute}}{E_U}}{h_m \cdot (x_{n-n,i} - \alpha_i)} \tag{12}$$

The strain at the bottom face is computed assuming plane sections with the cutoff limit at $\varepsilon_{Utu}$ because the softening material behavior is not taken into account

$$\varepsilon_{Uti} = \frac{f_{Ute}}{E_U} \cdot \left(1 + \frac{\alpha_i}{x_{n-n,i} - \alpha_i}\right) \tag{13}$$

Using the obtained strain distribution and assumed material properties, the stresses on the bottom and upper faces of the plate are computed, denoted $\sigma_{Uti}$ and $\sigma_{Uci}$, respectively. The deflection $\delta_i$ is calculated by transforming Eq. (4). The bending moment $M_i$ is found by transforming Eq. (8) with respect to the sectional equilibrium determined by Eq. (9), and the resultant force $F_i$ is computed using Eq. (5).

In this way, a series of $F_i$-$\delta_i$ pairs is plotted against the load–deflection curve obtained from testing. The first point ($\alpha_i = 0$) is Point A, from which the elastic limit stress $f_{Ute}$ and modulus of elasticity $E_u$ are found. The point at which the two curves diverge is Point B. By varying $\varepsilon_{Utu}$ such that the measured and computed curves are similar and Point B is shifted as far as possible toward the peak force, the inverse analysis is completed.

**R-UHPFRC Members**. Principles of Method 1 for plates are adopted for R-UHPFRC flexural members. After recording the force–deflection ($F$-$\delta$) curve during the test, the secant modulus $E_i$ at each measurement point is calculated. The material remains elastic, and thus $\alpha = 0$, and Eq. (9) yields $\lambda = 1$. Taking Eq. (4), and by analogy with Eq. (8) the following equation is obtained:

$$E_i = \frac{23 \cdot l_m^2 \cdot F_i \cdot (l_m - b_m)}{864 \cdot \delta_i \cdot I} \tag{14}$$

where $b_m$ = distance between load application points; and $I$ = inertia of beam in elastic state. Similar to the method for plate specimens, Point A is found, and the stress on the bottom face, i.e., the elastic limit stress $f_{Ute}$, is obtained using Euler–Bernoulli elastic beam theory.

At Point C, the position of the neutral axis $x_{n-n}$ needs to be located to obtain the tensile strength $f_{Utu}$. For each type of beam, $x_{n-n}$ is found separately, using extensometers installed over the height of beam. When the position is known, and under the assumption of elastic material response in compression and elastic-plastic response in tension [Fig. 3(b)], $f_{Utu}$ is found respecting the cross-sectional force balance and the acting bending moment at Point C.

Instead of finding Point B, another method is used for the determination of $\varepsilon_{Utu}$. In R-UHPFRC members, due to the composite action of both materials and the favorable orientation of fibers in the vicinity of the rebar, the tensile properties of UHPFRC are significantly better than those of nonreinforced elements. The tensile strain–hardening domain and thus the $\varepsilon_{Utu}$ value increases up to 5 times when B500B rebar is used (Leutbecher and Fehling 2012; Oesterlee 2010). By analogy with the simplified elastic-plastic material model from the Swiss standard SIA 2052 (Swiss Society of Engineers and Architects 2017), it is assumed that the tensile strain–hardening value of the UHPFRC is equal to $2\varepsilon_{Utu}$. This was validated by finite element modeling of the discussed R-UHPFRC beams, in which under a strain of $2\varepsilon_{Utu}$ in critical cross section, 97% of the ultimate resistance was achieved on average for the three types of beams.

## Finite-Element Modeling

Inverse analysis using FEM is based on finding a material model such that the computed and experimental structural response are in good agreement, and is used to verify results and assumptions of an analytical inverse analysis (Denarié et al. 2017). DIANA FEA 2017 software was used, as in Sadouki et al. (2017).

A two-dimensional (2D) model of the plate specimen subjected to four-point bending was built using plane-stress rectangular 5 × 5-mm finite elements. The UHPFRC was modeled as a continuum. The elastic, strain-hardening, and bilinear softening material response was simulated using an elastic multidirectional fixed-crack model. The material remained elastic until $f_{Ute}$ was reached. Then the stress–deformation curve was defined for strain hardening and postpeak softening responses. The localization of a fictitious crack along the element was determined by dividing the constant bending moment area into 20-mm-wide vertical zones. One of them, corresponding to the location of the critical section in the tested specimen, was modeled using the nominal material properties, whereas the rest of the plate was modeled using the material model with the same modulus of elasticity $E_U$, elastic limit stress $f_{Ute}$, and hardening modulus $E_{UH}$, but with higher tensile strength $f_{Utu}$. The constitutive law of UHPFRC including the beginning of the softening branch was varied until obtaining a similar force–deflection response as in the experiment. By observation of the first part of the force–deflection curve, $E_U$ and $f_{Ute}$ were adjusted iteratively. Observing further segments of the curve, $E_{UH}$, $f_{Utu}$, and finally the softening response were determined. The experiment was modeled until the ultimate member resistance was reached using a nonlinear solver with variable loading steps. The load introduction as displacement by means of nonlinear springs that acted in compression only reflected the possibility of loss of contact between the testing machine and the plate.

A similar method was used for modeling the R-UHPFRC beams. The T-shaped cross-section was modeled by division of the 2D model into six horizontal parts. The uppermost part represented the flange, and the remaining five parts composed the web. The variable web thickness was modeled through stepwise variation of the thickness such that the error of the moment of inertia of the beam was below 1%. The longitudinal rebars were modeled as straight, horizontal, perfectly anchored bars. Additionally, to avoid crushing of singular elements over the supports, 200-mm-long and 20-mm-thick steel plates were added, respecting the theoretical static scheme of the beam. The finite-element size was same as for the plates, i.e., 5 × 5 mm.





Downloaded from ascelibrary.org by Ecole Polytechnique Federale de Lausanne on 01/20/22. Copyright ASCE. For personal use only; all rights reserved.

Only the material model of the UHPFRC was fitted. The material properties of the rebars were adopted as elastic-perfectly plastic using the average material properties obtained from testing for each type of beam (Table 2).

### Material Model of UHPFRC

UHPFRC is a composite material made of a cementitious matrix and fibers. Due to this bicomponent structure, UHPFRC has quasi bilinear behavior under direct tension before reaching its tensile strength (Fig. 4).

The first stage is elastic. The behavior of UHPFRC is linear with Young's modulus $E_U$ and after unloading the strain comes back to zero.

After the elasticity limit [$f_{Ute}$ and $\varepsilon_{Ute}$ (Fig. 4)] is reached, uniformly distributed discontinuities in the matrix start to occur and the UHPFRC enters the strain-hardening domain with strain-hardening secant $E_{Uh}$ defined by Eq. (11). From the macroscopic point of view, the material can be considered as a continuum; however, it become increasingly anisotropic as hardening develops.

When UHPFRC is in the strain-hardening domain, after unloading, the residual strain $\varepsilon_{\text{res}}$ remains. When the tensile strength $f_{Utu}$ is reached, the unloading secant is calculated as

$$E_{Uu} = \frac{f_{Utu}}{k_u \cdot \varepsilon_{Utu}} \tag{15}$$

where $k_u = 0.5$ for UHPFRC with straight steel fibers (Wille and Naaman 2010). Under renewed tensile action, the response follows $E_{Uu}$ until the previously imposed stress is reached. If the tensile stress is increased further, the material follows the strain-hardening curve envelope in Fig. 4.

This work assumed that the unloading secant $E_{Ui}$ varies linearly from $E_U$ to $E_{Uu}$ between $\varepsilon_{Ute}$ and $\varepsilon_{Utu}$, respectively, which agrees with the behavior of fiber-reinforced mortar at the onset of matrix cracking (Visalvanich and Naaman 1981). To the authors' best knowledge, no research has studied the behavior of UHPFRC in compression after previously reaching the strain-hardening domain in tension. Tensile strain–hardening cement-based composites with steel fibers seem to follow unloading secant $E_{Ui}$ in the first stage of compressive response (Müller and Mechtcherine 2016), and this was adopted in the present work.

The UHPFRC in compression, without preloading in tension, behaves linear elastically with $E_U$ up to the compressive strength $f_{Uc}$.

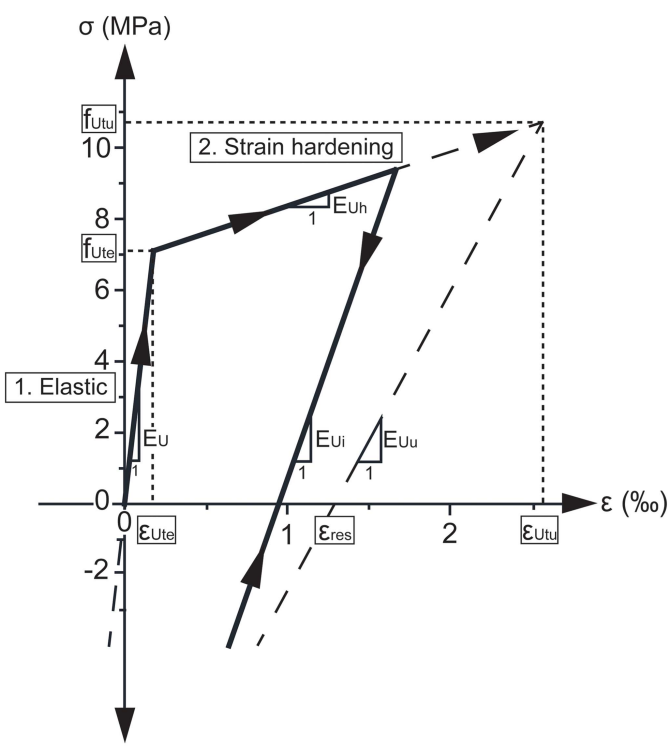


**Fig. 4.** Simplified UHPFRC constitutive law under loading–unloading in tension.

### Calculation of Stress Distribution in Cross Section

The stress distribution in the R-UHPFRC beam was computed using Euler–Bernoulli elastic beam theory and numerical methods. A perfect bond between the reinforcement bar and the UHPFRC was assumed (Oesterlee 2010).

The UHPFRC cross section of the beam was discretized into 100 horizontal layers of equal thickness, and the strain in each layer was assumed to be uniform. The elastic strain–hardening material model in tension and the perfectly elastic model in compression were adopted for UHPFRC during the first loading. The elastic–perfectly plastic model was adopted for the steel reinforcement bar.

The linear strain distribution is governed by the strain $\varepsilon$ in the bottom of member and by the position of the neutral axis $x_{n-n}$. For a given $x_{n-n}$, strain distribution in the UHPFRC and rebar was calculated. Based on the material model, stress in each layer and in the rebar was obtained. Resultant forces were computed with respect to the beam geometry. The neutral axis $x_{n-n}$ was determined when the sum of sectional forces was $\sum F = 0$. Then the resulting bending moment for the corresponding $\varepsilon$ was calculated. The procedure was automated in such a way that for a given bending moment, the unique pair of $\varepsilon$ and $x_{n-n}$ was found, and thus the distribution of stress was determined.

After the stress distribution for the maximum preloaded bending moment $M_{\max}$ was calculated, the unloading secants $E_{Ui}$ and residual strains $\varepsilon_{\text{res},i}$ depending on the reached stress were computed and stored for each UHPFRC layer. To find the strain distribution at the minimum unloaded bending moment $M_{\min}$, a new pair of $\varepsilon$ and $x_{n-n}$ was found. The UHPFRC layers that entered into the strain-hardening phase at $M_{\max}$ followed the unloading secant $E_{Ui}$ stored previously. Importantly, if in any layer the obtained strain was such that $0 < \varepsilon < \varepsilon_{\text{res},i}$, the stress in the UHPFRC was negative (i.e., compressive stress) despite a positive strain value (Fig. 4).

### Magnetic NDT

#### Principles of Magnetic NDT

The tensile strength of UHPFRC with steel fibers can be determined using nondestructive testing of the relative magnetic inductance. The distribution of tensile strength $f_{Utu}$ in an UHPFRC element depends on local orientation and content of fibers (Naaman 2018; Oesterlee et al. 2009), and can be approximated for straight fibers as follows (Hannant 1978; Naaman 1972):

$$f_{Utu} = \mu_0 \cdot \mu_1 \cdot \tau_f \cdot V_f \cdot \frac{l_f}{d_f} \tag{16}$$

where $\tau_f$ = average fiber pull-out stress; $V_f$, $l_f$, and $d_f$ = fiber volumetric content, length, and diameter, respectively; and $\mu_0$ and $\mu_1$ = fiber orientation and efficiency factors respectively.

The fiber orientation factor $\mu_0$ reflects the probability that a fiber crosses a given section. Under the assumption of homogenous fiber





Downloaded from ascelibrary.org by Ecole Polytechnique Federale de Lausanne on 01/20/22. Copyright ASCE. For personal use only; all rights reserved.

distribution, factor $\mu_0$ is determined as the ratio of the total area of fibers in the section to the fiber volume fraction (Krenchel 1975; Stroeven 2009)

$$\mu_0 = \frac{n_f \cdot A_f}{V_f} \tag{17}$$

The fiber efficiency factor $\mu_1$ considers the effect of angles between the fibers and a cross section of the composite (Oesterlee 2010; Wille et al. 2014) on the fibers' pull-out efficiency, and is dependent on $\mu_0$ (Bastien-Masse et al. 2016). Factor $\mu_0$ can be obtained precisely using image analysis of orthogonal surfaces of specimens extracted from structural members or accompanying elements for material testing (Oesterlee et al. 2009; Wuest 2007). It also can be assessed using nondestructive testing for sake of applicability in practice. The factor $\mu_1$ can be estimated on the basis of $\mu_0$ (Bastien-Masse et al. 2016; Nunes et al. 2017).

Because most UHPFRCs use steel fibers, their magnetic inductance $L$ can be exploited to establish $\mu_0$ and $V_f$ directly, and $\mu_1$ indirectly (Nunes et al. 2016, 2017). After measuring the magnetic inductance on the element surface in two directions, and the inductance of the air, ($L_x$, $L_y$, and $L_{\text{air}}$, respectively) the magnetic permeability is found as

$$\mu_{r,i} = \frac{L_i}{L_{\text{air}}} \tag{18}$$

Using the linear dependence of mean magnetic permeability $[\mu_{r,\text{mean}} = (\mu_{r,x} + \mu_{r,y})/2]$ on fiber content and since the matrix with no fibers ($V_f = 0\%$) has the permeability $\mu_{r,\text{mean}} = 0$, the slope of linear regression is determined. This slope is dependent on the type of fiber used (Pimentel and Nunes 2016), and subsequently is used to calculate the local $V_f$ at the measurement point. Slope values ranging from 3.8 to 4.55 are given in the literature (Nunes et al. 2016; Shen and Brühwiler 2020).

Using the fiber orientation factor $(\rho_x - \rho_y)$, $\mu_0$ and $\mu_1$ are obtained (Nunes et al. 2017)

$$(\rho_x - \rho_y) = 0.5\frac{\mu_{r,x} - \mu_{r,}}{\mu_{r,\text{mean}} - 1} \tag{19}$$

$$\mu_0 = 0.57 + 1.85(\rho_x - \rho_y) \tag{20}$$

$$\mu_1 = \begin{cases} 1.686 \cdot \sqrt{\mu_0} - 0.406, & \mu_0 < 0.7 \\ 1.0, & \mu_0 \geq 0.7 \end{cases} \tag{21}$$

## Magnetic NDT Calibration

Because the magnetic permeability of UHPFRC depends on the fiber type (Nunes et al. 2016), the calibration for the UHPFRC mix used in this research was performed. The sensor used in this research consisted of a ferritic U-shaped core with 28 × 30-mm cross section, 93 mm width, and 76 mm height. Two coils were made of 0.5-mm copper wire with about 170 turns each and were connected together (Fig. 5). The electrical inductance was measured using a LCR meter. Due to the circular magnetic flux produced in the U-shaped sensor, a certain effective depth is penetrated depending on the power of the magnetic field. For a sensor similar to the one used in the present study, but with smaller operating voltage (0.1 V), the effective depth was found to be equal to 25 mm (Li et al. 2018). Because according to Lenz's law the inductance is proportional to electromotive force, it can be expected that the effective depth increases with higher voltage in the coil. If the effective depth of the sensor is higher than the thickness of element used for calibration, the method cannot be used for elements of a different

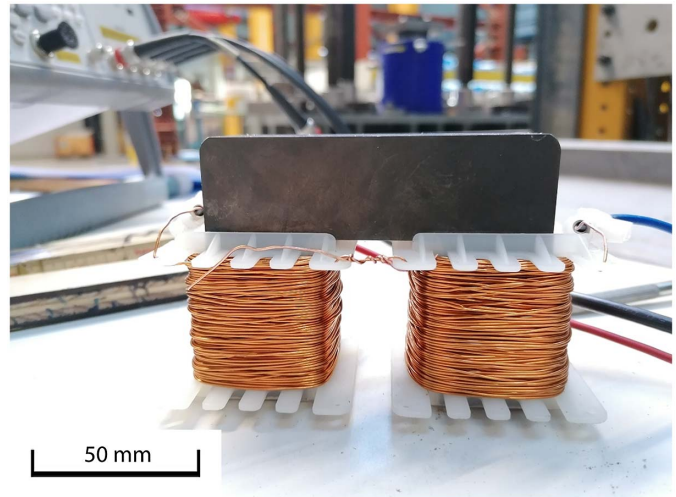


**Fig. 5.** Magnetic sensor used for NDT of UHPFRC tensile resistance.

thickness. In this study, 2 V current was chosen, as in Nunes et al. (2016); thus it was decided to perform the calibration on specimens specially prepared for this purpose instead of the plates used for material testing (30-mm thick).

Four plates 40 × 200 × 1,500 mm were cast vertically to mock-up the web of the T-shaped beam (Fig. 6). To assure nonuniformity of fiber alignment and distribution, and to obtain more calibration points for the method, four different methods of casting were applied: (1) casting from the top at one end, with no vibrating; (2) casting from the top at one end, with vibrating after casting; (3) casting from the top at one end, with vibrating during and after material placing; and (4) casting from the top at two ends, with vibrating during and after material placing.

After 28 days, the magnetic inductance was measured along the plates in two directions. The plates were cut to obtain six specimens from each plate (Fig. 6, a–f) with dimensions similar to the bending tensile test specimen according to Swiss standard SIA 2052 (Swiss Society of Engineers and Architects 2017), which were tested under four-point bending (Fig. 1) to obtain $f_{Utu}$ by means of inverse analysis, as described previously. Despite the greater thickness than that of the standard specimens, the same stress distribution at ultimate resistance was assumed (Shen et al. 2020).

Assuming an average $V_f = 3.8\%$ in all specimens, the slope of the regression curve was determined according to Nunes et al. (2016) to be equal to 4.59. Because the magnetic measurements on webs of T-shaped beams under the same assumption yielded average slopes of 4.64, it was accepted that

$$\mu_{r,\text{mean}} = 1 + 4.6V_f \tag{22}$$

Importantly, no correlation between the web thickness of T-beams and fitted slopes could be found. This confirms that the effective depth of the sensor was smaller than the thickness of plate used for calibration.

After finding the local $V_f$ and the factors $\mu_0$ and $\mu_1$ for measurement points at the critical section of tested plates, fiber pull-out shear stress for this kind of mix was estimated. Using Eq. (16), $\tau_f = 7.5$ MPa, which corresponds well to values obtained in pull-out test of fibers with the same diameter (6.9–10 MPa) (Orange et al. 2000; Wuest 2007). The method therefore was calibrated for the present UHPFRC mix, and could be used for $f_{Utu}$ calculation. The results obtained with destructive and nondestructive values during calibration for all 24 specimens are presented in Fig. 7.





Downloaded from ascelibrary.org by Ecole Polytechnique Federale de Lausanne on 01/20/22. Copyright ASCE. For personal use only; all rights reserved.

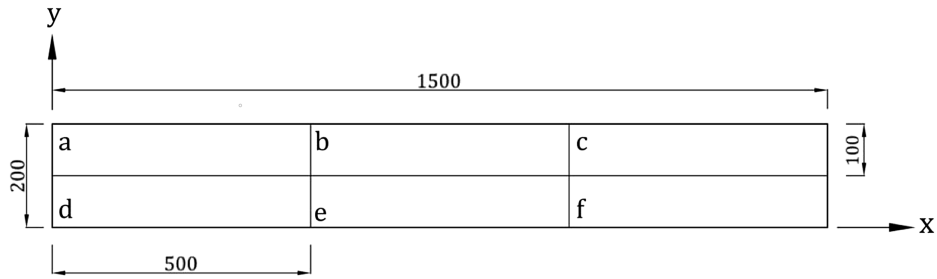


**Fig. 6.** Plates used for calibration of magnetic NDT method.

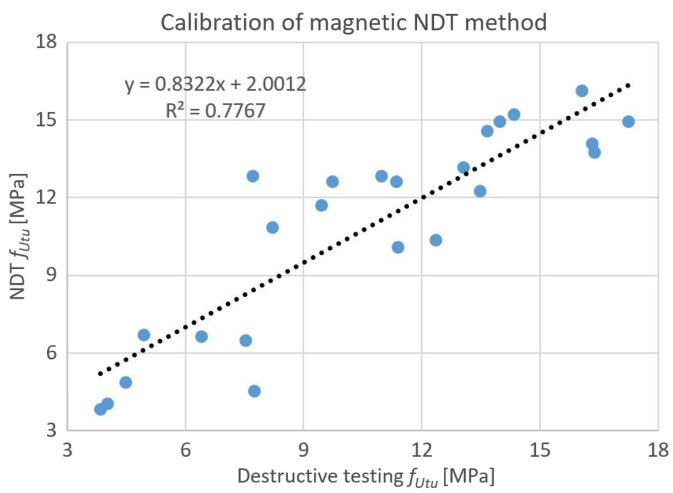


**Fig. 7.** Calculation of tensile resistance $f_{Utu}$ using calibrated magnetic NDT.

The rather large scatter of $f_{Utu}$ was due to the different casting methods, and should not be associated with material variation in the T-shaped beams.

## UHPFRC Properties

### *Comparison of FEM and Analytical Methods for Inverse Analysis of Plates*

For some of the plates tested in four-point bending, finite-element modeling was used to verify agreement between the two analytical inverse analysis methods. Representative specimens for each group were chosen. Specimens with critical cross sections close to the midspan were favored because the two analytical methods should be more precise at this location, and thus the comparison more reliable. The comparison of material properties obtained for 9 of plates total 48 from different castings at 28 and 90 days using 3 methods is presented in Table 3.

The elastic limit stress $f_{Ute}$ obtained with FEM was between the values obtained with the analytical methods (except in Plate 6). This also was found for strain hardening deformation $\varepsilon_{Utu}$ (except in Plates 3 and 7). Similar ultimate tensile strength $f_{Utu}$ was obtained with all methods; the variation was less than 15%.

The discrepancy between results obtained with each method illustrates the difficulty of fitting Point A in the analytical inverse analysis procedure. FEM should give the most precise results because the critical crack was modeled exactly where it appeared. Furthermore, the full sectional stress distribution was obtained, instead of a simplified distribution. Because the results obtained with FEM were between results of analytical analysis, it can be stated that the two methods approached the solution from two sides. The importance of these discrepancies is discussed subsequently.

### *Limit of Elasticity and Modulus of Elasticity*

The Young's modulus $E_U$ and elastic limit stress $f_{Ute}$ obtained with inverse analysis of all tested plates are presented in Table 4. The average values for each type of beam tested to failure also is given. The mean values ($\mu$) and standard deviations ($\sigma$) were computed for six plates in each test series after 28 and 90 days to quantify the scatter of results.

Comparison of the results shows that no change of properties occurred between 28 and 90 days age. Only the $f_{Ute}$ values obtained with Method 2 for Group 2 were the two mean values outside

**Table 3.** Tensile properties of UHPFRC obtained for nine plate specimens using analytical methods and finite-element modeling

| | Method 1 | | | | Method 2 | | | | FEM | | | |
|---|---|---|---|---|---|---|---|---|---|---|---|---|
| Plate | $f_{Ute}$ (MPa) | $f_{Utu}$ (MPa) | $\varepsilon_{Utu}$ (‰) | $E_U$ (GPa) | $f_{Ute}$ (MPa) | $f_{Utu}$ (MPa) | $\varepsilon_{Utu}$ (‰) | $E_U$ (GPa) | $f_{Ute}$ (MPa) | $f_{Utu}$ (MPa) | $\varepsilon_{Utu}$ (‰) | $E_U$ (GPa) |
| 1 | 5.5 | 13.2 | 3.6 | 43.7 | 10.0 | 13.2 | 2.0 | 42.0 | 9.0 | 13.5 | 2.2 | 43.7 |
| 2 | 9.5 | 12.5 | 2.3 | 43.3 | 8.5 | 12.5 | 1.3 | 46.0 | 9.5 | 13.0 | 1.9 | 43.3 |
| 3 | 6.1 | 12.1 | 5.6 | 43.1 | 9.0 | 12.1 | 3.5 | 43.5 | 6.5 | 12.1 | 2.6 | 43.1 |
| 4 | 6.0 | 9.0 | 1.5 | 42.0 | 8.0 | 9.0 | 1.2 | 42.0 | 6.0 | 7.5 | 1.5 | 42.0 |
| 5 | 4.3 | 10.2 | 3.3 | 40.2 | 7.9 | 10.2 | 2.2 | 40.0 | 6.5 | 10.2 | 2.8 | 40.2 |
| 6 | 3.5 | 10.7 | 3.7 | 45.2 | 4.0 | 10.7 | 1.2 | 43.0 | 5.0 | 10.5 | 1.4 | 43.0 |
| 7 | 4.1 | 8.6 | 1.1 | 33.8 | 4.0 | 8.6 | 0.8 | 35.0 | 4.1 | 9.0 | 0.5 | 33.8 |
| 8 | 3.8 | 12.2 | 4.1 | 40.2 | 8.2 | 12.2 | 2.4 | 34.0 | 6.0 | 14.0 | 3.2 | 40.2 |
| 9 | 5.9 | 13.5 | 4.2 | 40.0 | 7.0 | 13.5 | 2.5 | 38.0 | 7.0 | 15.0 | 3.0 | 40.0 |

Note: $f_{Ute}$ = elastic limit stress; $f_{Utu}$ = tensile strength; $\varepsilon_{Utu}$ = strain-hardening strain; and $E_U$ = modulus of elasticity.





Downloaded from ascelibrary.org by Ecole Polytechnique Federale de Lausanne on 01/20/22. Copyright ASCE. For personal use only; all rights reserved.

**Table 4.** Modulus of elasticity and elastic limit stress obtained for beams and plates using analytical and finite-element modeling methods

| | | Plate analytical method type | | | | | | | | Beams | | | |
|---|---|---|---|---|---|---|---|---|---|---|---|---|---|
| | | Method 1 | | Method 2 | | Method 1 | | Method 2 | | Analytical | FEM | Analytical | FEM |
| | | $f_{Ute}$ (MPa) | $f_{Ute}$ (MPa) | $f_{Ute}$ (MPa) | $f_{Ute}$ (MPa) | $E_U$ (GPa) | $E_U$ (GPa) | $E_U$ (GPa) | $E_U$ (GPa) | | | | |
| Type | Age | $\mu$ | $\sigma$ | $\mu$ | $\sigma$ | $\mu$ | $\sigma$ | $\mu$ | $\sigma$ | $f_{Ute}$ (MPa) | | $E_U$ (GPa) | |
| 1 | 28 days | 6.4 | 0.6 | 8.3 | 1.5 | 41.9 | 1.5 | 43.8 | 3.4 | 8.3 | 10.1 | 36.0 | 36.0 |
| | 90 days | 6.2 | 1.6 | 7.7 | 1.8 | 41.9 | 2.3 | 42.4 | 3.7 | | | | |
| 2 | 28 days | 5.5 | 1.0 | 6.8 | 0.6 | 39.5 | 2.9 | 40.2 | 2.8 | 9.8 | 9.0 | 37.7 | 36.5 |
| | 90 days | 4.2 | 0.6 | 4.3 | 0.6 | 41.3 | 3.1 | 42.0 | 2.7 | | | | |
| 3 | 28 days | 3.7 | 0.5 | 7.2 | 3.2 | 37.8 | 2.5 | 35.2 | 1.8 | 4.4 | 3.7 | 30.5 | 31.8 |
| | 90 days | 5.1 | 1.0 | 7.6 | 0.7 | 39.3 | 2.0 | 37.0 | 3.0 | | | | |

Note: $f_{Ute}$ = elastic limit stress; $E_U$ = modulus of elasticity; $\mu$ = mean value; and $\sigma$ = standard deviation.

the $2\sigma$ interval, indicating a scatter that was larger than expected assuming normal distribution of properties.

The elastic limit stress $f_{Ute}$ for plates was smaller than that for beams, confirming the beneficial influence of reinforcement on material properties (Oesterlee 2010). In contrast, the $E_U$ obtained was higher for plates than for beams. This may be explained by the neglected shear deformation in the calculation of deflection in inverse analysis.

Inverse analysis Method 2 for plates have in average 36% higher elastic limit stress $f_{Ute}$ than did Method I; the case of Type 3 casting after 28 days, this parameter almost doubled. This may be have been due to lack of rapid loss of stiffness or to regaining it at a later stage due to the fiber orientation and content stratification in the specimen. The moduli of elasticity $E_U$ found with the two methods were similar, and the average scatter was less than 1%.

The elasticity limit of Type 3 beams was lower than that of other types. This probably was caused by early age shrinkage cracking due to (1) lower matrix tensile resistance because of age of premix (>1 year); and (2) addition of omega stirrups, which changed the restrain level of the setting mix. Only in this group of beams were localized microcracks detected after spraying with alcohol before loading. Such defects are not considered in inverse analysis; a lower apparent elasticity limit and thus elastic limit stress are obtained. This group of beams was cast 1 year after the other specimens, with the same material.

### *Tensile Strength*

The tensile strength $f_{Utu}$ and hardening strain $\varepsilon_{Utu}$ obtained with inverse analysis of plates are presented in Table 5 together with values obtained for respective beams. The average value for each type of beam tested to failure is given. The mean values ($\mu$) and standard deviations ($\sigma$) are given for each series of tests after 28 and 90 days to quantify the scatter of results.

The mean $f_{Utu}$ for beams obtained with magnetic NDT and on the basis of $\tau_f$ retrieved previously for the current UHPFRC is presented in Table 5 as well. The average value for each beam was taken because the influence of fiber nonuniformity is negligible for the overall resistance of the beam (Pimentel and Nunes 2016) in R-UHPFRC members. Still, it determines the failure crack location (Sawicki and Brühwiler 2019).

The estimated hardening strain $\varepsilon_{Utu}$ was about 50% lower using the analytical inverse analysis Method 2 than using Method I. In the case of beams, larger $\varepsilon_{Utu}$ values were obtained with the analytical method than with the FEM method.

Similar $f_{Utu}$ values for plates and beams were obtained with all methods except Type 3 beams. As mentioned previously, due to the early age cracking, the apparent material strength was lower in the beams from this group.

## Ultimate Resistance of Members

To quantify the influence of variation of material properties obtained with different methods, the computed ultimate resistance of the beams was compared with the testing results. The simplified method from the Swiss UHPFRC standard SIA 2052 (Swiss Society of Engineers and Architects 2017) was used (Fig. 8), where $\sigma_{Uc}$ is compressive stress resulting from strain distribution, and $F_{Uc}$, $F_{Ut}$, and $F_s$ are resultant forces from compressive and tensile action of the UHPFRC and tensile action of the reinforcement bar, respectively.

The method assumes that the plain sections remain plain and that both reinforcement and UHPFRC in tension are fully activated.

**Table 5.** Tensile strength and hardening strain obtained for beams and plates using analytical and finite-element modeling methods and nondestructive testing

| | | Plate analytical method type | | | | | | Beams | | | | |
|---|---|---|---|---|---|---|---|---|---|---|---|---|
| | | | | Method 1 | | Method 2 | | Analytical | FEM | NDT | Analytical | FEM |
| | | $f_{Utu}$ (MPa) | | $\varepsilon_{Utu}$ (MPa) | $\varepsilon_{Utu}$ (MPa) | $\varepsilon_{Utu}$ (GPa) | $\varepsilon_{Utu}$ (GPa) | | | | | |
| Type | Age | $\mu$ | $\sigma$ | $\mu$ | $\sigma$ | $\mu$ | $\sigma$ | $f_{Utu}$ (MPa) | | | $\varepsilon_{Utu}$ (GPa) | |
| 1 | 28 days | 11.8 | 2.1 | 3.6 | 1.5 | 2.1 | 1.0 | 12.7 | 12.8 | 13.0 | 3.8 | 2.7 |
| | 90 days | 12.3 | 2.0 | 3.4 | 1.0 | 1.6 | 0.5 | | | | | |
| 2 | 28 days | 10.6 | 0.7 | 3.4 | 1.0 | 1.5 | 0.4 | 11.8 | 11.2 | 11.6 | 2.2 | 2.6 |
| | 90 days | 11.1 | 0.8 | 4.0 | 1.0 | 1.3 | 0.2 | | | | | |
| 3 | 28 days | 11.6 | 2.8 | 2.6 | 1.4 | 1.6 | 0.8 | 7.3 | 7.3 | 9.1 | 2.9 | 2.4 |
| | 90 days | 12.0 | 1.5 | 3.4 | 0.9 | 2.1 | 0.5 | | | | | |

Note: $f_{Utu}$ = tensile strength; $\varepsilon_{Utu}$ = strain-hardening strain; $\mu$ = mean value; and $\sigma$ = standard deviation.





Downloaded from ascelibrary.org by Ecole Polytechnique Federale de Lausanne on 01/20/22. Copyright ASCE. For personal use only; all rights reserved.

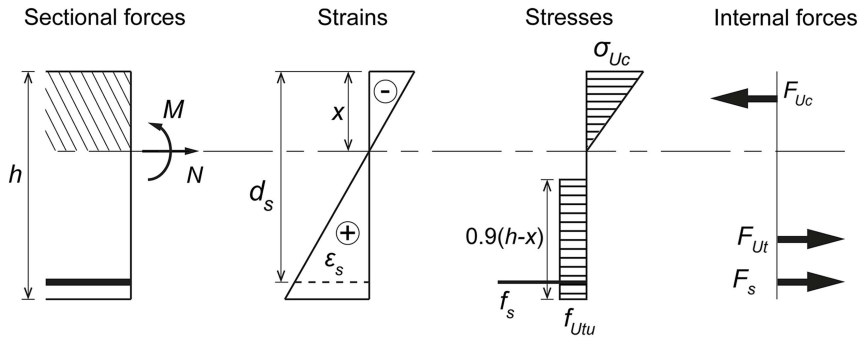


**Fig. 8.** Simplified resistance model for UHPFRC members to determine the ultimate resistance, according to SIA 2052 (Swiss Society of Engineers and Architects 2017).

The tensile stress block of UHPFRC is taken as 90% of height below the neutral axis to consider the fact that part of the material is in the elastic state. Then the neutral axis can be found to comply with force balance in the cross section. For the sake of comparison, the mean values of resistance were used here. As mentioned previously, strain at the bottom of the beam was assumed to be equal to $2\varepsilon_{Utu}$ by analogy to SIA 2052 (Swiss Society of Engineers and Architects 2017), and supported by FEM simulations. For values based on magnetic NDT, the $\varepsilon_{Utu}$ and $Eu$ mean values obtained from plates using Method 1 for the respective types of beams were adopted. To quantify the composite behavior of reinforcement and UHPFRC, the ratio $Q$ of the sectional tensile force shared between them is presented in Table 6.

The bending resistance based on material testing for Groups 1 and 2 consistently was below the experimental value of ultimate resistance, but within a 10% margin, thus showing good agreement. For Group 3, the ultimate resistance was overestimated by 20% due to the previously mentioned early age shrinkage cracking of the matrix. Importantly, the ultimate resistance values determined using the $f_{Utu}$ value obtained by NDT were closer than those based on values from material testing. This was because the fiber orientation and content variation can be grasped correctly by the NDT method. The ultimate resistance based on the inverse analysis of beams is shown for the sake of comparison to quantify the error of the model. Finally, the smaller rebars (Ø20 mm) contributed as much as the UHPFRC to the tensile sectional force, and the contribution of UHPFRC decreased with increase of rebar diameter to 34 mm.

**Table 6.** Experimental and calculated bending resistance of beams

| Beam/ method | Test (kNm) | Method 1 (kNm) | Method 2 (kNm) | NDT (kNm) | Beam analysis (kNm) | $Q$ |
|---|---|---|---|---|---|---|
| Type 1 | 109.2 | 107.8 | 105.2 | 110.2 | 108.9 | 0.98:1 |
| Type 2 | 230.4 | 213.6 | 203.4 | 217.1 | 228.8 | 1.54:1 |
| Type 3 | 82.2 | 97.7 | 95.5 | 89.1 | 86.1 | 0.94:1 |

Note: $Q$ = tensile force carried by reinforcement and UHPFRC ratio.

## Stress Distribution in Members under Service Conditions

Two additional beams, one of Type 2 with Ø34 mm rebar and one of Type 3 with Ø20 mm rebar, were tested to investigate flexural stiffness and stress distribution in the cross section under service conditions. They were instrumented with strain gauges on the rebars prior to casting. Multiple loading–unloading cycles were imposed to simulate structural response under possible service conditions, up to about 50% of ultimate resistance (S). Figs. 9 and 10 present measured force vs strain and calculated stress distribution for Type 2 beam (Ø34 mm) respecitvely, while Figs. 11 and 12 present the same information for Type 3 beam (Ø20 mm).

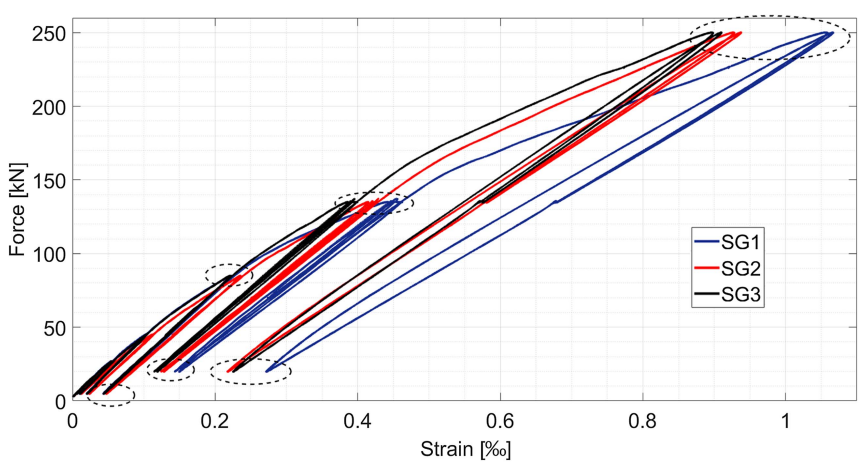


**Fig. 9.** Force versus strain in reinforcement in Type 2 beam (Ø34 mm) for three strain gauges (SGs) glued on rebar. Dashed ellipses denote modeled load steps.





Downloaded from ascelibrary.org by Ecole Polytechnique Federale de Lausanne on 01/20/22. Copyright ASCE. For personal use only; all rights reserved.

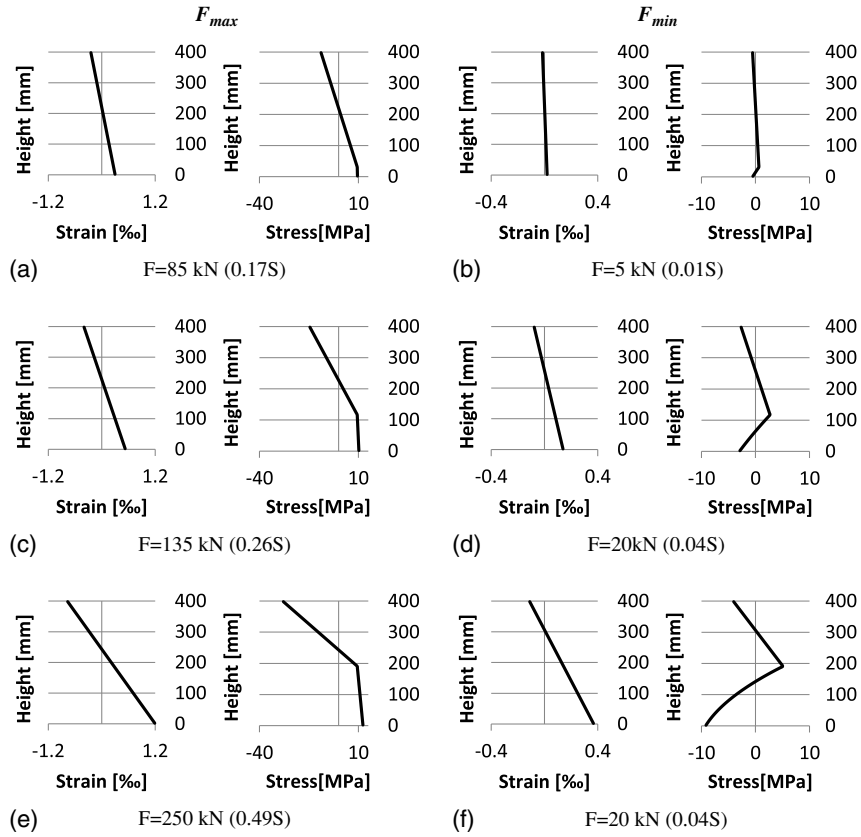


**Fig. 10.** Stress and strain distribution in UHPFRC during loading ($F_{\max}$) and unloading ($F_{\min}$) for Type 2 beam (Ø34 mm).

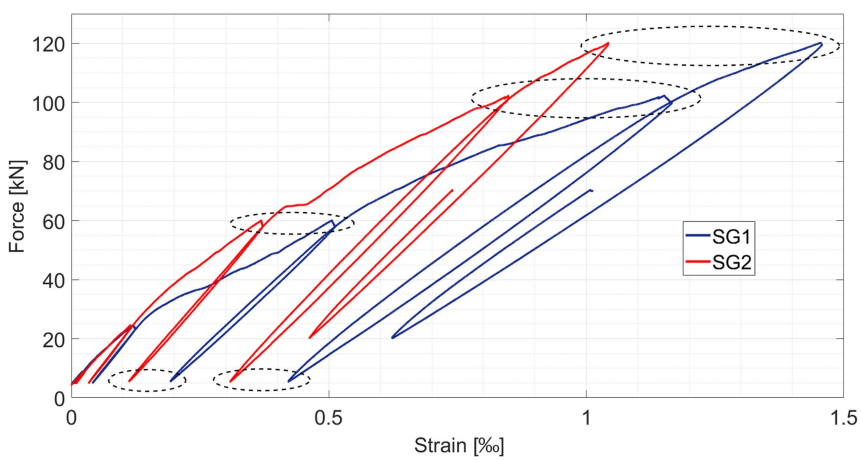


**Fig. 11.** Force versus strain in reinforcement in Type 3 beam (Ø20 mm) for two stain gauges (SGs) glued on rebar. Dashed ellipses denote modeled load steps.

Figs. 9 and 11 present the measured strain variation in the rebar during the test. The scatter in the measured values probably was due to the variation of the UHPFRC properties in the members. Similar variation was observed by other researchers (Makita and Brühwiler 2014; Oesterlee et al. 2009; Toutlemonde et al. 2013).

The results of member modeling are presented in Tables 7 and 8. The structural response of the beams was calculated using the material properties obtained from plates with the two methods of analytical inverse analysis, and with the inverse FEM analysis of beams. Good agreement of the modeled and the measured reinforcement bar strains were obtained, validating the method. Because the beams used for validation were not those used to obtain the material properties, it is demonstrated that the method can be applied to structural members.

The residual strain after loading–unloading leads to increased stress in reinforcement bars under a given force. For beams of Type 2, stress in the reinforcement under loading of 20 kN doubled, from about 31 to 60 MPa, when preloaded to a force level of 135 or 250 kN, respectively (Table 7). In the case of Type 3 beams, stress in the reinforcement under a force of 5 kN increased from about 35 to 85 MPa when previously loaded with 60 or 102 kN, respectively (Table 8).





Downloaded from ascelibrary.org by Ecole Polytechnique Federale de Lausanne on 01/20/22. Copyright ASCE. For personal use only; all rights reserved.

Downloaded from ascelibrary.org by Ecole Polytechnique Federale de Lausanne on 01/20/22. Copyright ASCE. For personal use only; all rights reserved.

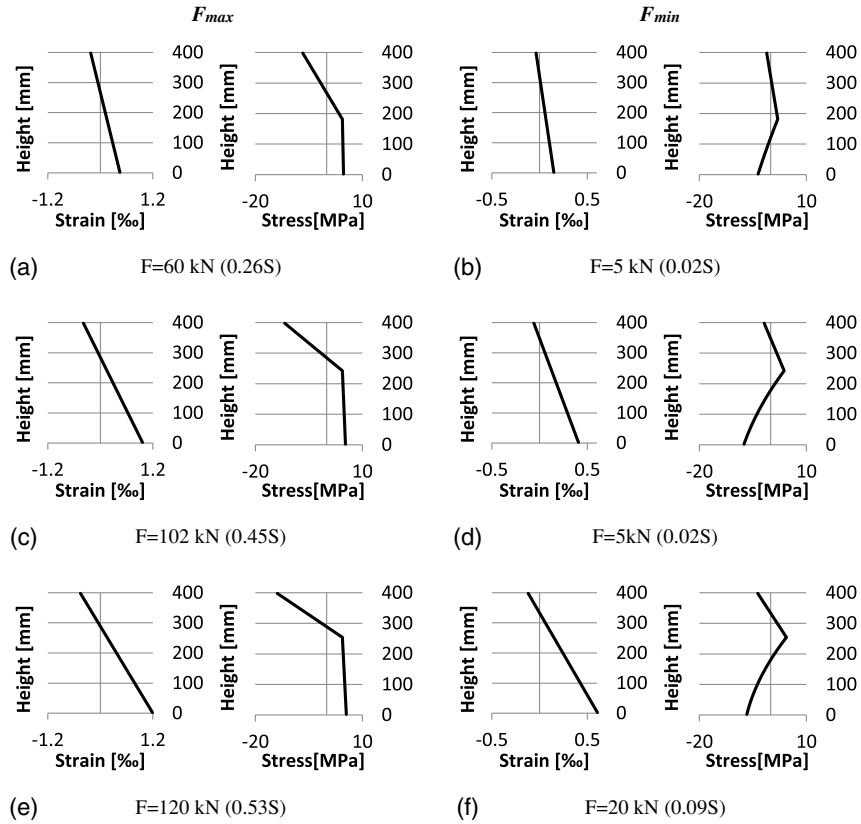


**Fig. 12.** Stress and strain distribution in UHPFRC during loading ($F_{\max}$) and unloading ($F_{\min}$) for Type 3 beam (Ø20 mm).

**Table 7.** Validation of stress distribution Type 2 (Ø34 mm)

| Force (kN) | $S$ | Strain (%) modelled in rebar, UHPFRC properties from inverse analysis: Beams | Method 1 | Method 2 | Strain measured in rebar (%) | Stress measured in rebar (MPa) | $Q$ | $R$ |
|---|---|---|---|---|---|---|---|---|
| 85 | 0.17 | 0.25 | 0.30 | 0.27 | 0.22–0.23 | 54–56 | 0.63:1 | 0.91 |
| 5 | 0.01 | 0.02 | 0.09 | 0.06 | 0.04 | 10 | 0.73:1 | 1.00 |
| 135 | 0.26 | 0.45 | 0.57 | 0.52 | 0.39–0.44 | 96–108 | 0.79:1 | 0.81 |
| 20 | 0.04 | 0.12 | 0.26 | 0.19 | 0.12–0.14 | 29–34 | 1.25:1 | 0.98 |
| 250 | 0.49 | 1.03 | 1.24 | 1.12 | 0.89–1.05 | 218–257 | 1.28:1 | 0.75 |
| 20 | 0.04 | 0.32 | 0.56 | 0.37 | 0.22–0.27 | 54–66 | 2.10:1 | 0.97 |

Note: $S$ = load to ultimate load ratio; $Q$ = tensile force carried by reinforcement and UHPFRC ratio; and $R$ = strain-hardening to elastic inertia ratio.

**Table 8.** Validation of stress distribution Type 3 (Ø20 mm)

| Force (kN) | $S$ | Strain modeled in rebar, UHPFRC properties from inverse analysis of (%): Beams | Method 1 | Method 2 | Strain measured in rebar (%) | Stress measured in rebar (MPa) | $Q$ | $R$ |
|---|---|---|---|---|---|---|---|---|
| 60 | 0.26 | 0.42 | 0.37 | 0.28 | 0.36–0.50 | 84–117 | 0.57:1 | 0.59 |
| 5 | 0.02 | 0.12 | 0.14 | 0.04 | 0.11–0.19 | 26–44 | 0.90:1 | 0.84 |
| 102 | 0.45 | 0.90 | 0.82 | 0.65 | 0.84–1.14 | 196–267 | 0.98:1 | 0.53 |
| 5 | 0.02 | 0.39 | 0.39 | 0.20 | 0.31–0.42 | 72–98 | 1.56:1 | 0.84 |
| 120 | 0.53 | 1.13 | 1.03 | 0.84 | 1.04–1.45 | 243–339 | 1.16:1 | 0.53 |
| 20 | 0.09 | 0.57 | 0.56 | 0.36 | 0.46–0.62 | 108–145 | 2.18:1 | 0.82 |

Note: $S$ = load to ultimate load ratio; $Q$ = tensile force carried by reinforcement and UHPFRC ratio; and $R$ = strain-hardening to elastic inertia ratio.

The ratio $Q$ of tensile sectional force carried by the reinforcement bar and the UHPFRC describes the level of cooperation between them. As stress increases and the UHPFRC enters the strain-hardening domain, the load bearing contribution of the rebar increases. After unloading at $F_{\min}$, the rebar contribution is more pronounced than during loading to $F_{\max}$ due to difference in loading ($E_U$ and $E_{Uh}$) and unloading ($E_{Ui}$) secant values of the UHPFRC. The variation of the ratio $Q$ is due to modification of the cross-sectional properties due to the strain hardening and unloading constitutive laws of UHPFRC. This mechanism greatly

reduces the stress variation in the rebar during loading–unloading cycles, which is particularly important in the case of fatigue.

Loss of member stiffness was quantified with the $R$-ratio of bending inertia of the cross section showing UHPFRC strain-hardening to initial elastic inertia. The moment of inertia was calculated separately for $F_{\max}$ and $F_{\min}$ in each cycle. For $F_{\max}$, a composite cross section with three moduli of elasticity was assumed (AFGC 2013): (1) UHPFRC in the elastic state with $E_U$, (2) UHPFRC in the strain-hardening state with $E_{Uh}$, and (3) the reinforcement bar with $E_s$. The moment of inertia was calculated with respect to the neutral axis position $x_{n-n}$ at $F_{\max}$. For calculation of member inertia at unloading, the secant $E_{Ui}$ was calculated for each computational layer separately. Then, the inertia of the composite cross section about $x_{n-n}$ at $F_{\max}$ was obtained. The inertia at $F_{\min}$ was higher than at $F_{\max}$, which is reflected by the slopes of the curves in Figs. 9 and 11.

The distribution of strain and stress in the UHPFRC for each load step is presented in Figs. 10 and 12. The response at $F_{\min}$ depended on the stress distribution at $F_{\max}$. Interestingly, the UHPFRC in the bottom part of the member, which usually is in tension, may even have higher compressive stresses than the upper part when the beam is unloaded, depending on geometrical dimensions and loading history. In the case of the presented T-shaped beams, the bottom part was contributing as much as 90% of total compressive sectional force [Fig. 10(f)]. Similar behavior, but with smaller compressive stress activated because of a different cementitious material used, was observed by Wang et al. (2020). With increasing load, the neutral axis position moves up due to strain-hardening and increase of $Q$. At unloading, the axis moves even higher, compared with the respective $F_{\max}$, due to the UHPFRC response, and especially when compressive stress is activated in the bottom part of section.

The aforementioned mechanism determines the structural response and should be taken into account when calculating the stress state of a member under service conditions. During loading, the range of elastic limit stress $f_{Ute}$ in the cross section should be found and the modified composite section should be taken into account for stress calculations. When the structure is unloaded, a more complex method should be applied, with calculation of $E_{Ui}$. However, because stiffness during unloading is higher than that at primary loading, neglecting the modified moment of inertia at unloading is acceptable for the sake of simplification, leading to a higher computed deflection range, and thus to a conservative solution. Nevertheless, modified inertia at unloading should be taken into account during monitoring of deflection of R-UHPFRC structures under service loading, as well as calculation of stress ranges under fatigue actions.

The method was validated for both beam types, and good agreement was obtained between measured and calculated strain using material properties obtained from inverse analysis of beams. The agreement with properties based on plate testing was lower, with an average error of 20%. It is not obvious which method of inverse analysis of plates gives better results for the beam in the service state.

This paper analyzed test results of R-UHPFRC members and UHPFRC plates subjected to four-point bending. Using magnetic nondestructive testing and inverse analysis principles based on analytical and finite-element models, the UHPFRC material properties were determined. The results were compared, and the importance of their variation was quantified for R-UHPFRC beam under loading–unloading in the service state and at ultimate resistance.

This research showed that:

- The analytical inverse analysis methods also can be used for structural elements, such as full-scale beams, including elements with reinforcement bars; correctness of the results was confirmed by finite-element modeling.
- UHPFRC in the tensile zone of R-UHPFRC member enters into compression if it previously was loaded beyond the elasticity limit. This phenomenon leads to significantly increased tensile strain in the rebar in the unloaded state, and thus influences the global response of the structural member. This increase is notable in particular at high loading levels, and should be taken into account during design and verification of structures.
- Magnetic NDT allows determining the UHPFRC tensile strength $f_{Utu}$ when the average fiber pull-out stress of the UHPFRC mix is known. Better estimation of ultimate bending resistance of structural members is obtained than that based on material testing because fiber distribution in the element explicitly is taken into account. Therefore, this technique can be used to check the quality of elements.
- Magnetic NDT allows for determining only the tensile resistance, and therefore must be combined with material testing using small specimens to obtain the full set of material properties. This method gives results comparable to those of UHPFRC characterization with inverse analysis of a prototype element, and thus can be considered as an alternative to testing of a prototype element.

Furthermore, the knowledge gap regarding the behavior of UHPFRC in tension–compression regimes was identified. It is recommended that this research topic should be investigated, which in turn would allow improving the quality of modeling of R-UHPFRC members under loading–unloading in the serviceability domain.

## Data Availability Statement

Some or all data, models, or code that support the findings of this study are available from the corresponding author upon reasonable request (models, measurements and computations).

## Acknowledgments

This project has received funding from the European Union's Horizon 2020 research and innovation program under the Marie Skłodowska-Curie Grant Agreement No. 676139–INFRASTAR.

## References

Adel, M., K. Nagai, and K. Matsumoto. 2019. "Simplified design approach of steel fiber reinforced concrete under flexural load." In *Proc., 10th Int. Conf. on Fracture Mechanics of Concrete and Concrete Structures*. Bayonne, France: International Association of Fracture Mechanics for Concrete and Concrete Structures. https://doi.org/10.21012/FC10.234838.

AFGC (Association Francaise de Genie Civil). 2013. *Ultra high performance fibre-reinforced concretes*. Recommendations, Revised edition, June 2013. Documents scientifiques et techniques (édition AFGC). Paris: AFGC.

Azmee, N. M., and N. Shafiq. 2018. "Ultra-high performance concrete: From fundamental to applications." *Case Stud. Constr. Mater.* 9 (Dec): e00197. https://doi.org/10.1016/j.cscm.2018.e00197.

Baby, F., B. Graybeal, P. Marchand, and F. Toutlemonde. 2013. "UHPFRC tensile behavior characterization: Inverse analysis of four-point bending test results." *Mater. Struct.* 46 (8): 1337–1354. https://doi.org/10.1617/s11527-012-9977-0.

Baril, M. A., L. Sorelli, J. Réthoré, F. Baby, F. Toutlemonde, L. Ferrara, S. Bernardi, and M. Fafard. 2016. "Effect of casting flow defects on the crack propagation in UHPFRC thin slabs by means of stereovision





Downloaded from ascelibrary.org by Ecole Polytechnique Federale de Lausanne on 01/20/22. Copyright ASCE. For personal use only; all rights reserved.

digital image correlation." *Constr. Build. Mater.* 129 (Dec): 182–192. https://doi.org/10.1016/j.conbuildmat.2016.10.102.

Barnett, S. J., J.-F. Lataste, T. Parry, S. G. Millard, and M. N. Soutsos. 2010. "Assessment of fibre orientation in ultra high performance fibre reinforced concrete and its effect on flexural strength." *Mater. Struct.* 43 (7): 1009–1023. https://doi.org/10.1617/s11527-009-9562-3.

Bastien-Masse, M., E. Denarié, and E. Brühwiler. 2016. "Effect of fiber orientation on the in-plane tensile response of UHPFRC reinforcement layers." *Cem. Concr. Compos.* 67 (Mar): 111–125. https://doi.org/10.1016/j.cemconcomp.2016.01.001.

Brühwiler, E. 2016. "'Structural UHPFRC': Welcome to the post-concrete era!" In *Proc., Int. Interactive Symp. on Ultra-High Performance Concrete*. Des Moines, IA: Iowa State University Digital Press.

Brühwiler, E., H. Friedl, C. Rupp, and H. Escher. 2019. "Bau einer Bahnbrücke aus bewehrtem UHFB." *Beton- Stahlbetonbau* 114 (5): 337–345. https://doi.org/10.1002/best.201900010.

BSI (British Standard Institution). 2005. *Eurocode 2: Design of concrete structures-Part 1-1: Genera rules and rules for buildings*. London: BSI.

Denarié, E., L. Sofia, and E. Brühwiler. 2017. "Characterization of the tensile response of strain hardening UHPFRC—Chillon viaducts." In *Proc., AFGC-ACI-fib-RILEM Int. Symp. on Ultra-High Performance Fibre-Reinforced Concrete, UHPFRC 2017—Pro 106*, 242–250. Montpellier, France: RILEM.

de Oliveira e Sousa, J. L. A., and R. Gettu. 2006. "Determining the tensile stress-crack opening curve of concrete by inverse analysis." *J. Eng. Mech.* 132 (2): 141–148. https://doi.org/10.1061/(ASCE)0733-9399(2006)132:2(141).

Farhat, F. A., D. Nicolaides, A. Kanellopoulos, and B. L. Karihaloo. 2007. "High performance fibre-reinforced cementitious composite (CARDIFRC): Performance and application to retrofitting." *Eng. Fract. Mech.* 74 (1–2): 151–167. https://doi.org/10.1016/j.engfracmech.2006.01.023.

Gao, D., Z. Gu, J. Tang, and C. Zhang. 2020. "Fatigue performance and stress range modeling of SFRC beams with high-strength steel bars." *Eng. Struct.* 216 (Aug): 110706. https://doi.org/10.1016/j.engstruct.2020.110706.

Graybeal, B., E. Brühwiler, B.-S. Kim, F. Toutlemonde, Y. L. Voo, and A. Zaghi. 2020. "International perspective on UHPC in bridge engineering." *J. Bridge Eng.* 25 (11): 04020094. https://doi.org/10.1061/(ASCE)BE.1943-5592.0001630.

Habel, K., E. Denarié, and E. Brühwiler. 2007. "Experimental investigation of composite ultra-high-performance fiber-reinforced concrete and conventional concrete members." *ACI Struct. J.* 104 (1): 93.

Habel, K., M. Viviani, E. Denarié, and E. Brühwiler. 2006. "Development of the mechanical properties of an ultra-high performance fiber reinforced concrete (UHPFRC)." *Cem. Concr. Res.* 36 (7): 1362–1370. https://doi.org/10.1016/j.cemconres.2006.03.009.

Hannant, P. J. 1978. *Fibre cements and fibre concretes*. Chichester, UK: Wiley.

Huang, B.-T., Q.-H. Li, S.-L. Xu, and L. Zhang. 2019. "Static and fatigue performance of reinforced concrete beam strengthened with strain-hardening fiber-reinforced cementitious composite." *Eng. Struct.* 199 (Nov): 109576. https://doi.org/10.1016/j.engstruct.2019.109576.

Krenchel, H. 1975. "Fibre spacing and specific fibre surface." *Fibre Reinforced Cem. Concr.* 1975: 69–79.

Leutbecher, T., and E. Fehling. 2012. "Tensile behavior of ultra-high-performance concrete reinforced with reinforcing bars and fibers: Minimizing fiber content." *Struct. J.* 109 (2): 253–264.

Li, L., J. Xia, and I. Galobardes. 2018. *Magnetic probe to test spatial distribution of steel fibres in UHPFRC prisms*. Melbourne, Australia: Federation Internationale du Beton.

López, J. Á., P. Serna, J. Navarro-Gregori, and E. Camacho. 2015. "An inverse analysis method based on deflection to curvature transformation to determine the tensile properties of UHPFRC." *Mater. Struct.* 48 (11): 3703–3718. https://doi.org/10.1617/s11527-014-0434-0.

López, J. Á., P. Serna, J. Navarro-Gregori, and H. Coll. 2016. "A simplified five-point inverse analysis method to determine the tensile properties of UHPFRC from unnotched four-point bending tests." *Composites, Part B* 91 (Apr): 189–204. https://doi.org/10.1016/j.compositesb.2016.01.026.

Makita, T., and E. Brühwiler. 2014. "Tensile fatigue behaviour of ultra-high performance fibre reinforced concrete (UHPFRC)." *Mater. Struct.* 47 (3): 475–491. https://doi.org/10.1617/s11527-013-0073-x.

MCS (Laboratory of Maintenance and Safety of Structures) EPFL (École Polytechnique Fédérale de Lausanne). 2020. "UHPFRC map Switzerland." Accessed July 17, 2020. https://www.epfl.ch/labs/mcs/mcs-laboratory-for-maintenance-and-safety-of-structures/uhpfrc-map-switzerland/.

Mezquida-Alcaraz, E. J., J. Navarro-Gregori, and P. Serna-Ros. 2019. "Numerical validation of a simplified inverse analysis method to characterize the tensile properties in strain-softening UHPFRC." In Vol. 596 of *Proc., IOP Conf. Series: Materials Science and Engineering*, 012006. Bristol, UK: IOP Publishing.

Müller, S., and V. Mechtcherine. 2016. "Behaviour of strain-hardening cement-based composites (SHCC) under force-controlled cyclic loading." In *Proc., 9th Int. Conf. on Fracture Mechanics of Concrete and Concrete Structures, IA-FraMCoS*. Bayonne, France: International Association of Fracture Mechanics for Concrete and Concrete Structures. https://doi.org/10.21012/FC9.169.

Naaman, A. E. 1972. *A statistical theory of strength for fiber reinforced concrete*. Boston: Massachusetts Institute of Technology.

Naaman, A. E. 2018. *Fiber reinforced cement and concrete composites*. Sarasota, FL: Techno Press.

Nunes, S., M. Pimentel, and A. Carvalho. 2016. "Non-destructive assessment of fibre content and orientation in UHPFRC layers based on a magnetic method." *Cem. Concr. Compos.* 72 (Sep): 66–79. https://doi.org/10.1016/j.cemconcomp.2016.05.024.

Nunes, S., M. Pimentel, F. Ribeiro, P. Milheiro-Oliveira, and A. Carvalho. 2017. "Estimation of the tensile strength of UHPFRC layers based on non-destructive assessment of the fibre content and orientation." *Cem. Concr. Compos.* 83 (Oct): 222–238. https://doi.org/10.1016/j.cemconcomp.2017.07.019.

Oesterlee, C. 2010. "Structural response of reinforced UHPFRC and RC composite members." Doctoral thesis, Laboratory of Maintenance and Safety of Structures, École polytechnique fédérale de Lausanne.

Oesterlee, C., E. Denarié, and E. Brühwiler. 2009. "Strength and deformability distribution in UHPFRC panels." In *Proc., of 4th Int. Conf. on Construction Materials: Performance, Innovations and Structural Implications ConMat'09*, 390–397. Tokyo: Japan Concrete Institute.

Orange, G., J. Dugat, and P. Acker. 2000. "Ductal®: New ultra high performance concretes. Damage resistance and micromechanical analysis." In *Proc., 5th RILEM Symp. on Fibre-Reinforced Concrete (FRC)*, 781–790. Paris: RILEM.

Pan, R., E. Brühwiler, and X. Shen. 2016. *Nonlinear numerical analysis of R-UHPFRC railway* Π*-beams*. Paris: RILEM.

Pimentel, M., and S. Nunes. 2016. "Determination of the fibre content and orientation in UHPFRC layers using NDT—Application to the simulation of the behaviour of strengthened beams." In *Maintenance, monitoring, safety, risk and resilience of bridges and bridge networks*. London: Taylor & Francis.

Qian, S., and V. C. Li. 2008. "Simplified inverse method for determining the tensile properties of strain hardening cementitious composites (SHCC)." *J. Adv. Concr. Technol.* 6 (2): 353–363. https://doi.org/10.3151/jact.6.353.

Qiu, M., X. Shao, K. Wille, B. Yan, and J. Wu. 2020. "Experimental investigation on flexural behavior of reinforced ultra high performance concrete low-profile T-beams." *Int. J. Concr. Struct. Mater.* 14 (1): 5. https://doi.org/10.1186/s40069-019-0380-x.

Rossi, P., D. Daviau-Desnoyers, and J.-L. Tailhan. 2015. "Analysis of cracking in steel fibre-reinforced concrete (SFRC) structures in bending using probabilistic modelling." *Struct. Concr.* 16 (3): 381–388. https://doi.org/10.1002/suco.201400081.

Sadouki, H., E. Denarié, and E. Brühwiler. 2017. "Validation of a FEA model of structural response of RC-cantilever beams strengthened with a (R-) UHPFRC layer." *Constr. Build. Mater.* 140 (Jun): 100–108. https://doi.org/10.1016/j.conbuildmat.2017.02.090.

Sawicki, B., and E. Brühwiler. 2019. "Static behavior of reinforced UHPFRC beams with minimal cover thickness." In *Proc., 2IIS-UHPC—The 2nd Int. Interactive Symp. on Ultra-High Performance Concrete*. Albany, IA: Iowa State University Digital Press.

Downloaded from ascelibrary.org by Ecole Polytechnique Federale de Lausanne on 01/20/22. Copyright ASCE. For personal use only; all rights reserved.

Shen, X., and E. Brühwiler. 2020. "Influence of local fiber distribution on tensile behavior of strain hardening UHPFRC using NDT and DIC." *Cem. Concr. Res.* 132 (Jun): 106042. https://doi.org/10.1016/j.cemconres.2020.106042.

Shen, X., E. Brühwiler, and W. Peng. 2020. "Biaxial flexural response of Strain-Hardening UHPFRC circular slab elements." *Constr. Build. Mater.* 255 (Sep): 119344. https://doi.org/10.1016/j.conbuildmat.2020.119344.

SIA 262. 2014. *Concrete structures*. SIA 262:2014. Zurich, Switzerland: Swiss Society of Engineers and Architects.

Stroeven, P. 2009. "Stereological principles of spatial modeling applied to steel fiber-reinforced concrete in tension." *ACI Mater. J.* 106 (3): 213–222.

Swiss Society of Engineers and Architects. 2017. *UHPFRC: Materials, design and construction*. SIA 2052. Zurich, Switzerland: Swiss Society of Engineers and Architects.

Tailhan, J.-L., P. Rossi, and E. Parant. 2004. "Inverse numerical approach to determine the uniaxial tensile behaviour of a stress hardening cement composite from its bending behaviour." In *Proc., 6th Int. RILEM Symp.: Fiber Reinforced Concretes—BEFIB 2004*, 914–922. Paris: RILEM.

Toutlemonde, F., A. Simon, P. Rivillon, P. Marchand, F. Baby, M. Quiertant, A. Khadour, J. Cordier, and T. Battesti. 2013. "Recent experimental investigations on reinforced UHPFRC for applications in earthquake engineering and retrofitting." In *Proc., UHPFRC 2013: Int. Symp. on Ultra-High Performance Fibre-Reinforced Concrete*, 597–606. Paris: RILEM.

Visalvanich, K., and A. Naaman. 1981. "Compliance measured fracture toughness of mortar and fiber reinforced mortar." In *Fracture mechanics for ceramics, rocks, and concrete*, edited by S. Freiman and E. Fuller, 141–156. West Conshohocken, PA: ASTM.

Wang, B., R. Fang, and Q. Wang. 2020. "Flexural behavior of fiber-reinforced self-stressing concrete T-shaped composite beams." *Adv. Civ. Eng.* 2020: e8810440. https://doi.org/10.1155/2020/8810440.

Wille, K., and A. E. Naaman. 2010. "Fracture energy of UHP-FRC under direct tensile loading." In *Fracture mechanics of concrete and concrete structures: Recent advances in fracture mechanics of concrete*, edited by B. H. Oh. Seoul: Korea Concrete Institute.

Wille, K., N. V. Tue, and G. J. Parra-Montesinos. 2014. "Fiber distribution and orientation in UHP-FRC beams and their effect on backward analysis." *Mater. Struct.* 47 (11): 1825–1838. https://doi.org/10.1617/s11527-013-0153-y.

Wuest, J. 2007. "Comportement structural des bétons de fibres ultra performants en traction dans des éléments composés." Doctoral thesis, Laboratory of Maintenance and Safety of Structures, Ecole polytechnique Federal de Lausanne.

Yang, I.-H., C. Joh, and T. Q. Bui. 2019. "Estimating the tensile strength of ultrahigh-performance fiber-reinforced concrete beams." *Adv. Mater. Sci. Eng.* 2019: 16. https://doi.org/10.1155/2019/5128029.

Yoo, D.-Y., and Y.-S. Yoon. 2016. "A review on structural behavior, design, and application of ultra-high-performance fiber-reinforced concrete." *Int. J. Concr. Struct. Mater.* 10 (2): 125–142. https://doi.org/10.1007/s40069-016-0143-x.

Downloaded from ascelibrary.org by Ecole Polytechnique Federale de Lausanne on 01/20/22. Copyright ASCE. For personal use only; all rights reserved.